Chemical Engineering Journal 509 (2025) 160939

Contents lists available at ScienceDirect

Chemical Engineering Journal

journal homepage: www.elsevier.com/locate/cej

Exploring calcium pillaring of O3-type $NaNi_{0.9}Ti_{0.1}O_2$ cathodes to advance Na-ion battery technology☆

Siyu An [a], Leonhard Karger [a], Philipp Müller [b], Jing Lin [a], Sami Vasala [c], Volodymyr Baran [d], Sören L. Dreyer [a], Ruizhuo Zhang [a], Fatih Ulusoy [a], Aleksandr Kondrakov [a,b,*], Jürgen Janek [a,e,*], Torsten Brezesinski [a,*]

[a] Battery and Electrochemistry Laboratory (BELLA), Institute of Nanotechnology, Karlsruhe Institute of Technology (KIT), Kaiserstr. 12, 76131 Karlsruhe, Germany
[b] BASF SE, Carl-Bosch-Str. 38, 67056 Ludwigshafen, Germany
[c] European Synchrotron Radiation Facility (ESRF), avenue des Martyrs 71, 38000 Grenoble, France
[d] Deutsches Elektronen-Synchrotron DESY, Notkestr. 85, 22607 Hamburg, Germany
[e] Institute of Physical Chemistry & Center for Materials Research (ZfM/LaMa), Justus-Liebig-University Giessen, Heinrich-Buff-Ring 17, 35392 Giessen, Germany

ARTICLE INFO

Keywords:
Sodium-ion battery
Cathode active material
Layered oxide
Substitution
Pillaring effect
Electro-chemo-mechanical degradation

ABSTRACT

$NaNi_{0.9}Ti_{0.1}O_2$ (NNTO), a promising sodium-ion cathode material, is capable of delivering high specific capacities but is compromised by structural degradation at high potentials and poor redox stability. Herein, we introduced varying amounts of Ca^{2+} as pillaring ions into the intercalation sites of NNTO to examine their effect on structure and electrochemical performance. Laboratory X-ray diffraction and charge/discharge testing identified $Na_{0.95}Ca_{0.025}Ni_{0.9}Ti_{0.1}O_2$ (CaNNTO) as the optimal composition in terms of interlayer spacing, rate capability, and cycling stability. Specifically, the capacity retention after 200 cycles improved from 27 to 48 %. To elucidate the role of Ca^{2+}, synchrotron X-ray diffraction was performed, revealing that CaNNTO undergoes only about 3 % volume change in the initial cycle, compared to about 30 % for NNTO. This reduced volume variation was confirmed by cross-sectional electron microscopy and acoustic emission measurements. Hard and soft X-ray absorption spectroscopy further indicated a more reversible nickel redox ($Ni^{2+}/Ni^{3+}/Ni^{4+}$) in CaNNTO, and differential electrochemical mass spectrometry demonstrated that Ca^{2+} incorporation helps suppress oxygen loss from the lattice, thereby directly stabilizing the cathode|electrolyte interface. Overall, calcium pillaring is found to effectively mitigate structural collapse and redox instabilities, making CaNNTO a more viable candidate for practical sodium-ion battery applications.

The significant challenges posed by the temporal and spatial discontinuities of renewable energy in practical applications require effective energy-storage devices that can be deployed at a mass scale. Since the 1990s, the development and commercialization of lithium-ion batteries (LIBs), pioneered by Sony Corp., significantly accelerated the progress of energy-storage technologies, which in turn has catalyzed the rapid growth of electric vehicles, including hybrid and plug-in hybrid vehicles [1–4]. However, the geographic distribution and relatively high costs of lithium resources have fueled the pursuit of a more sustainable solution. Sodium-ion batteries (SIBs) have therefore emerged as a promising next-generation technology, mainly because of their similarity to LIBs in many respects while using abundant sodium as the shuttling ion and also offering alternative concepts for cathode materials [5–7].

Among the various sodium intercalation and insertion compounds, layered oxides have garnered significant attention due to their favorable electrochemical properties and similarity to high-capacity $LiTMO_2$ (e.g., $LiNi_xCo_yMn_zO_2$, NCM or NMC) cathode materials employed in LIBs [6,8–11]. In contrast to LIBs, which are constrained by a limited selection of transition metal (TM) species, layered sodium-ion cathodes can be synthesized from a broader range of 3d TMs – from Ti to Cu [9–13]. This flexibility allows for the use of more abundant and sustainable elements, which can further reduce production costs.

O3 and P2 are known as two different thermodynamically stable structures of TM oxide cathode materials in SIBs. P2-type layered oxides have been widely studied due to their face-shared trigonal prismatic

☆ This article is part of a special issue entitled: 'Electrochemical Energy' published in Chemical Engineering Journal.

* Corresponding authors.
E-mail addresses: aleksandr.kondrakov@basf.com (A. Kondrakov), juergen.janek@kit.edu (J. Janek), torsten.brezesinski@kit.edu (T. Brezesinski).

https://doi.org/10.1016/j.cej.2025.160939

Available online 23 February 2025

alkali-metal sites, offering superior sodium transport properties compared to O3-type layered oxides [6,8,14,15]. O3-type oxides, by contrast, have a larger sodium inventory and are thus more suitable for full-cell applications. However, Na^+ extraction/intercalation from/into O3 phases typically leads to complex transitions and significant volume changes, which can induce microcracking and structural degradation [16–19]. Therefore, exploring strategies to improve the cycling performance of O3-type SIB cathode materials is of great importance.

A commonly employed strategy to enhance the performance of $NaTMO_2$ phases is elemental substitution. In our previous work, we successfully synthesized $NaNi_{0.9}Ti_{0.1}O_2$ (NNTO) by substitution of the nickel ions in $NaNiO_2$ (NNO) with 10 mol.% Ti^{4+} [20]. Although NNTO demonstrated significantly improved cycling stability and specific capacity compared to NNO, the prevailing O''3 → O1 phase transition at potentials above 4.0 V vs. Na^+/Na led to volume collapse and irreversible lattice oxygen loss, which ultimately compromised its cyclability. To address these issues, we implemented a pillaring strategy aimed at stabilizing the cathode material through the substitution of intercalation sites with Ca^{2+}, which has been shown to be an effective method for enhancing the electrochemical performance of layered oxides [21–28]. In this study, NNTO was substituted with varying amounts of Ca^{2+}. By comparing results from Rietveld refinements of X-ray diffraction (XRD) data and electrochemical testing, we identified 2.5 mol.% as the optimal Ca^{2+} fraction. Subsequently, further physical and electrochemical characterization techniques were employed to gain insight into the stabilization mechanism.

To explore the impact of different calcium contents on the structure and performance of NNTO, as well as to determine the solubility limit, a relatively wide range of concentrations was selected for investigation. To substitute NNTO with Ca^{2+}, different amounts of $Ca(OH)_2$ were added during the pre-calcination step to NaOH, $Ni(OH)_2$, and TiO_2, according to the stoichiometry of $Na_{1-2x}Ca_xNi_{0.9}Ti_{0.1}O_2$ (with x = 0.005, 0.01, 0.015, 0.02, 0.025, 0.03, 0.035, 0.04, 0.045, and 0.05). The mixture was then heated at 300 °C for 10 h under O_2 atmosphere to facilitate dehydration and ensure good contact between the reactants. The resulting product was homogenized and calcined at 800 °C for 12 h to obtain the layered material (see Experimental section for more details).

Subsequently, all ten samples were subjected to XRD analysis. The respective patterns are presented in Fig. 1**a**, and phase fractions from Rietveld refinements are shown in **Fig. S1** and further given in **Table S1**. It is evident that the main phase of all samples is of $R\bar{3}m$ symmetry, accompanied by varying fractions of an impurity phase with space group $Fm\bar{3}m$, which can be attributed to the presence of rock salt-like NiO and/or CaO. As the degree of substitution increases, the impurity fraction also increases, although CaO is not clearly visible in Fig. 1**a**. In the study of NNTO, the NiO content increased with a decreasing Na/TM ratio, and this trend also applies to the $Na_{1-2x}Ca_xNi_{0.9}Ti_{0.1}O_2$ samples employed in the present work [20]. The introduction of Ca^{2+} results in a sodium-deficient state, making the formation of NiO energetically more favorable. Notably, a significant increase in phase fraction of CaO is observed when the Ca^{2+} fraction reaches 2.5 mol.%, suggesting that this may be the solubility limit in the alkali-metal (intercalation) sites of NNTO.

Fig. 1**b** shows the refined structural parameters for the different materials (see also **Table S2**). The lattice parameters a and c, as well as the unit-cell volume, seemingly reach a local maximum at 2.5 mol.%. Subsequently, they exhibit a decreasing trend up to a Ca^{2+} fraction of about 4.0 mol.%, after which they increase again. It is worth noting that when Ca^{2+} is introduced as a pillaring ion into P2-type oxides, the c-parameter typically shows a contraction due to the smaller ionic radius of calcium and higher charge compared to sodium [27,28]. However, for O3-type oxides reported in the literature, the results are more complex. For example, in the study of Yu *et al.* on $Na_{0.98}Ca_{0.01}Ni_{0.5}Mn_{0.5}O_2$, the c-parameter decreased upon Ca^{2+} introduction, due to enhanced O^{2-}–Ca^{2+}–O^{2-} bonding in the layered lattice compared to O^{2-}–Na^+–O^{2-}. In contrast, for both $Na_{0.95}Ca_{0.025}Ni_{1/3}Fe_{1/3}Mn_{1/3}O_2$ and $Na_{0.9}Ca_{0.05}Ni_{1/3}Fe_{1/3}Mn_{1/3}O_2$, increases in c with Ca^{2+} substitution have been attributed to the formation of sodium vacancies [4,21,22,24]. The results of the current study align with the latter scenario, as the introduction of Ca^{2+} apparently leads to the generation of an equivalent number of sodium vacancies, thus resulting in an expansion of the interlayer spacing.

For the trend of an increasing a-parameter up to $x \approx 0.025$ in $Na_{1-2x}Ca_xNi_{0.9}Ti_{0.1}O_2$, the following hypothesis can be proposed. With increasing Ca^{2+} concentration, the fraction of NiO impurity phase also increases, which may lead to the formation of vacancies at the nickel sites. To compensate for the charge imbalance, more nickel ions are likely to be oxidized to Ni^{3+}. Unlike O^{2-}–TM–O^{2-}, in the vacancy configuration, the lack of shielding against O–O repulsion by the transition metals results in an increase in a. Considering that Ni^{3+} has a smaller ionic radius than Ni^{2+} (0.56 Å vs. 0.69 Å), the expansion effect dominates, leading to the observed increase in a-parameter.

In the range of $0.025 < x < 0.04$, the lattice parameters exhibit a decreasing trend, which may be attributed to Ca^{2+} reaching its solubility limit, leading to the formation of more sodium vacancies. As shown in **Fig. S1** and **Table S1**, the fraction of NiO impurity phase clearly increases within this range, leading to the oxidation of Ni^{2+} to Ni^{3+} for charge compensation. Consequently, the smaller ionic radius of Ca^{2+} (1.00 Å vs. 1.02 Å), along with its higher charge relative to Na^+, leads to

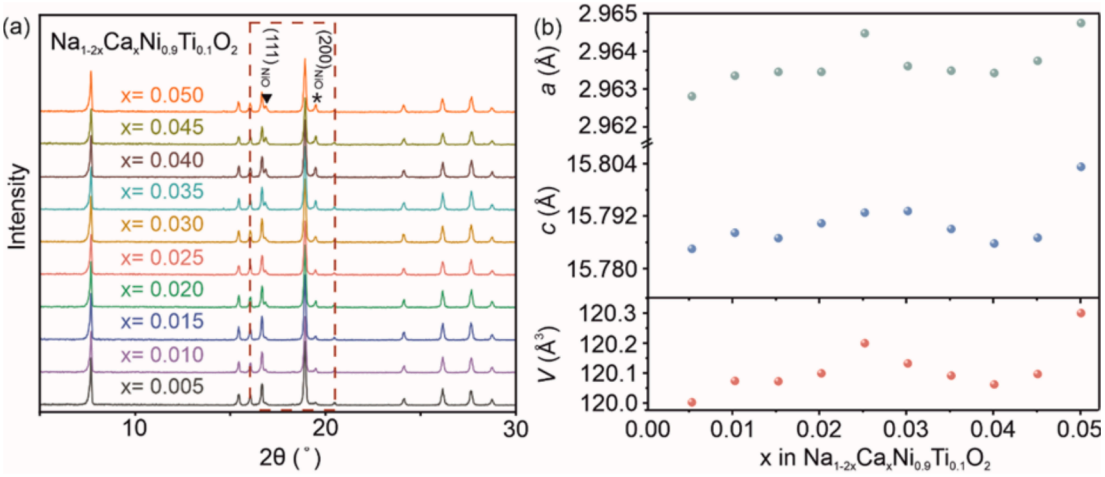

Fig. 1. (a) Laboratory XRD patterns collected from the $Na_{1-2x}Ca_xNi_{0.9}Ti_{0.1}O_2$ samples and (b) corresponding lattice parameters and unit-cell volumes from Rietveld refinement analyses.

a contraction of the interlayer spacing, and the increasing concentration of Ni^{3+} contributes to the decrease in *a*-parameter, thus resulting in a decrease in unit-cell volume. However, for $x > 0.04$, we hypothesize that further reduction in sodium content in the O^{2-}–Na^{+}–O^{2-} layers creates more vacancies, leading to the increase of O–O repulsion that outweighs the effects of Ca^{2+}. This results in an increase in lattice parameters *a* and *c*, as well as in unit-cell volume. A similar trend is also reflected in the interlayer spacing, as shown in **Fig. S2** (see also **Table S2**). Therefore, we selected the five samples with fractions below the apparent solubility limit, as well as that containing 5.0 mol.% Ca^{2+}, for subsequent scanning electron microscopy (SEM) analysis and electrochemical testing.

Fig. S3 shows SEM images of the aforementioned materials. As can be seen from this data, the primary particle size of all five samples is somewhat larger than that of NNTO, indicating that the introduction of Ca^{2+} promotes grain growth. However, among them, there is no significant difference in either primary particle size or morphology. In contrast, the sample with 5.0 mol.% Ca^{2+} exhibits a distinct morphology, characterized by the presence of nanoscale particles, which may be attributed to the deposition of excess CaO on the free surface of the primary and secondary particles, corroborating our hypothesis that the solubility limit of Ca^{2+} in NNTO is reached at $x \approx 0.025$.

Electrochemical performance testing in the potential window of 2.0–4.2 V vs. Na^{+}/Na was conducted to investigate differences between these samples. **Table S3** gives the results from inductively coupled plasma-optical emission spectroscopy (ICP-OES) measurements. Considering 2–3 mol.% sodium loss during calcination, all samples exhibit the expected stoichiometric ratios. The cyclability of SIB half-cells using the $Na_{1-2x}Ca_xNi_{0.9}Ti_{0.1}O_2$ cathodes is displayed in Fig. 2. It is noteworthy that, except for the 5.0 mol.% Ca^{2+} sample, the initial specific discharge capacities (see Fig. 2**a**) are similar. This indicates that similar amounts of Na^{+} ions are de/intercalated at a rate of C/30, which in turn suggests that moderate Ca^{2+} substitution barely affects the capacity. The fact that the sample with a Ca^{2+} fraction of 5.0 mol.% delivers a lower specific capacity can be attributed to two main factors. First, as mentioned earlier, the formation of NiO impurities (see also **Fig. S1**) may lead to vacancies at the nickel sites and defects in the $Na_{1-2x}Ca_xNi_{0.9}Ti_{0.1}O_2$ lattice. For maintaining charge balance, both the originally present 0.1 mol of Ni^{2+} and 0.8 mol of Ni^{3+} are getting oxidized, thereby reducing the number of available redox-active species. Additionally, the presence of CaO on the particle surface may hinder sodium diffusion (higher cathode|electrolyte impedance, etc.), which would ultimately negatively affect cyclability.

Fig. 2**b** presents the long-term performance at C/2, after formation at C/30 for five cycles. The capacity retentions after 200 cycles are about 32, 36, 42, 44, 48, and 42 % for the $Na_{1-2x}Ca_xNi_{0.9}Ti_{0.1}O_2$ cathodes with $x = 0.005$, 0.010, 0.015, 0.020, 0.025, and 0.050, respectively, much improved compared to NNTO (about 26 %). This may be attributed to the pillaring effect of Ca^{2+}, which helps maintain the interlayer spacing at high states of charge or, in other words, at high degrees of desodiation, thus preserving sodium diffusivity in the bulk phase. This is also reflected in the changes in overpotential during cycling. The overpotential decreases with increasing degree of Ca^{2+} substitution (up to $x = 0.025$), which agrees with the trend in capacity degradation seen in **Fig. S4**.

Furthermore, analysis of differential capacity curves (see **Fig. S5**) reveals that cells using the 2.5 mol.% Ca^{2+} sample exhibit a much lower polarization than those with NNTO, with the redox peaks being largely maintained after 200 cycles. In contrast, the curves for NNTO are virtually featureless from the 150th cycle onward. This indicates that Ca^{2+} incorporation not only facilitates sodium diffusion but also improves stability. The mechanisms underlying this behavior were probed, among others, using soft X-ray absorption spectroscopy (sXAS) and differential electrochemical mass spectrometry (DEMS).

Fig. 2**c** presents the rate-performance data. At the initial low rate of C/30, all samples are capable of delivering similar specific discharge capacities. However, with increasing rate, from C/10 to 2C, the $Na_{1-2x}Ca_xNi_{0.9}Ti_{0.1}O_2$ materials with $x = 0.010$, 0.015, 0.020, 0.025, and 0.050 reveal an overall better performance. Among them, those having Ca^{2+} fractions of 2.0 and 2.5 mol.% exhibit the best performance, characterized by higher specific capacities across various rates. NNTO and the sample containing 5.0 mol.% Ca^{2+} have inferior sodium diffusivity at rates $\geq$ C/2, leading to increased overpotential and poor performance. Surprisingly, the nanoscale particles detected on the surface of the 5.0 mol.% Ca^{2+} sample do not strongly affect its rate capability. When the SIB half-cells are returned to cycling with C/30 rate, the $Na_{1-2x}Ca_xNi_{0.9}Ti_{0.1}O_2$ materials recover toward high discharge capacities.

To better illustrate the effect of calcium pillaring on kinetics, the differential capacity curves for cells using the 2.5 mol.% Ca^{2+} sample and NNTO at rates ranging from C/30 to 2C are compared in **Fig. S6**. The data clearly demonstrate the enhanced rate performance of NNTO enabled by Ca^{2+} substitution, with consistently lower overpotentials across all current densities.

In summary, the 2.5 mol.% Ca^{2+} sample exhibits favorable structural parameters, the best capacity retention, and good rate capability. Therefore, this sample was selected for in-depth analysis and is referred to as CaNNTO in the following.

Fig. 3**a** presents the XRD data for CaNNTO obtained using synchrotron radiation, with the refined lattice parameters and phase fractions given in **Tables S4** and **S5**. The data are of better quality than those acquired by laboratory XRD, making them ideal for comparison with NNTO. Notably, the *a*- and *c*-parameters and the unit-cell volume are slightly larger compared to the laboratory XRD results, while the phase fractions are similar. The interslab distances, 5.2675 Å for CaNNTO and 5.2590 Å for NNTO, are indicated in Fig. 3**b**. As expected, calcium pillaring leads to an increase by about 0.16 %, which helps explain the superior cycling performance of CaNNTO.

Fig. 3**c** shows the results from energy-dispersive X-ray spectroscopy (EDS) analysis. The elemental maps indicate a relatively uniform

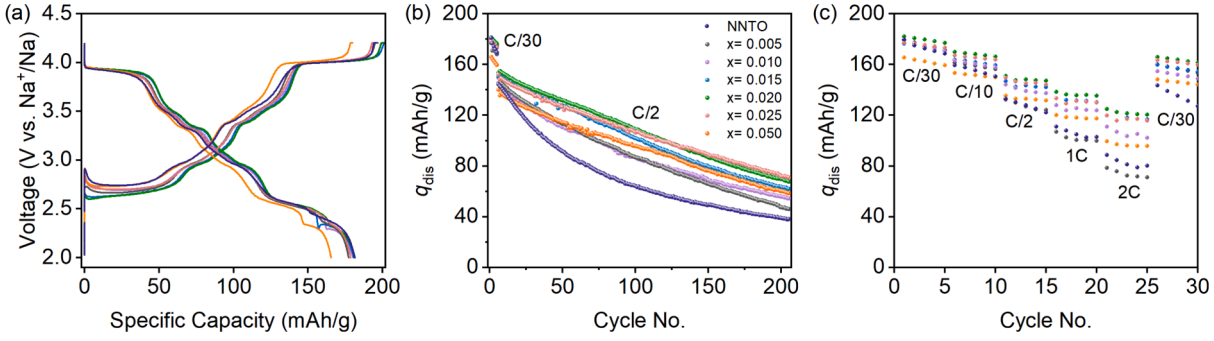

Fig. 2. (a) Voltage profiles at C/30, (b) long-term cycling performances at C/2, and (c) rate capabilities of $Na_{1-2x}Ca_xNi_{0.9}Ti_{0.1}O_2$ and NNTO cathodes in SIB half-cells.

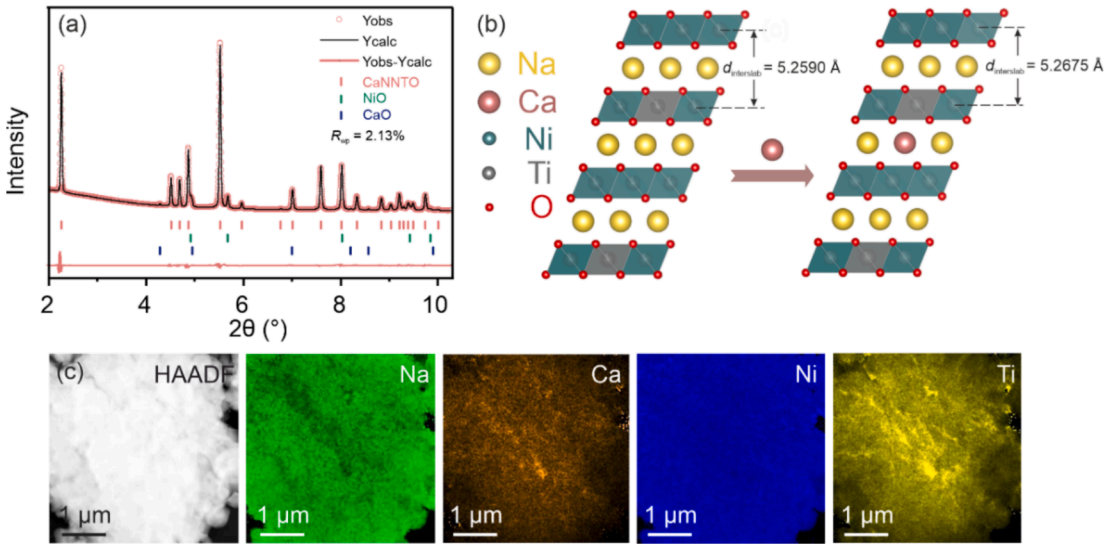

Fig. 3. (a) Rietveld refinement profile of synchrotron XRD data for CaNNTO. (b) Schematic representations of the crystal structures of CaNNTO and NNTO. The interlayer spacings are indicated. (c) STEM-EDS mapping of CaNNTO.

distribution of sodium and nickel. In contrast, some inhomogeneities are visible for calcium and titanium, increasing toward the center of the secondary particles. This finding is supported by the line scan results presented in **Fig. S7**. However, low-magnification EDS mapping (see **Fig. S8**) demonstrates a more uniform distribution of the respective elements. Aside from that, the measured stoichiometry (see **Table S3**) agrees well with the expected ratios, suggesting only local inhomogeneities in some of the particles. To address this issue in future studies, the co-precipitation method could be employed for achieving a more uniform distribution of calcium and titanium.

Figs. 4 and **S9** present atomic-resolution scanning transmission electron microscopy (STEM) images of CaNNTO taken in high-angle annular dark-field (HAADF) mode. Specifically, top- and side-view images are shown in Figs. 4**a** and **S9a**, clearly revealing the layered structure. This is confirmed by the fast Fourier transform (FFT) patterns extracted from the HAADF-STEM images (see Figs. 4**b** and **S9b**), indicating that the bulk structure is of well-ordered O3-type nature. Furthermore, the intensity line scans in Figs. 4**c** and **S9c** reveal lattice plane distances of 0.21 nm {104} and 0.26 nm {006}, respectively, which are in good agreement with the XRD results.

To provide a clearer comparison of the cyclability between CaNNTO and NNTO, their first-cycle voltage profile, long-term cycling performance, and rate capability are shown in **Fig. S10**. These aspects were already discussed above in detail, so they will not be elaborated further here.

To gain a better understanding of the structural evolution of

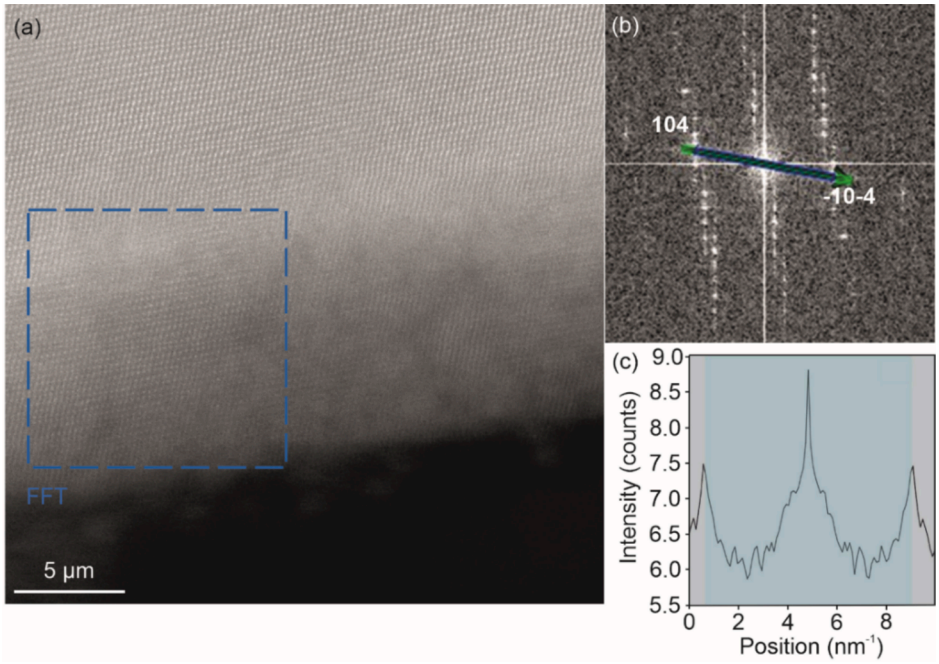

Fig. 4. (a) Atomic-resolution HAADF-STEM image of CaNNTO. (b) FFT pattern from the region indicated by the dashed blue box in (a). It should be noted that additional intensities are present along the vertical direction due to sample vibration artifacts. (c) Intensity line scan along the direction indicated by the arrow in (b). The distance of 0.21 nm corresponds to the {104} lattice planes of the layered phase. (For interpretation of the references to colour in this figure legend, the reader is referred to the web version of this article.)

CaNNTO during charging and discharging, *operando* synchrotron XRD measurements were conducted on the SIB half-cells, which resulted in the 2D contour plot shown in Fig. 5**a**. Starting from the initial O3 phase, the extraction of Na^+ ions leads to increased O–O repulsion in the O^{2-}–Na^+–O^{2-} layers, eventually resulting in the formation of a P3 phase at about 3.2 V in the first cycle at C/10 rate, as evidenced by the appearance of (003), (006), (101), (012), and (015) reflections. With further increase in state of charge, the P3 phase transitions toward an O'3 phase at about 4.0 V, which remains stable even at higher potentials, and then reverts back to P3 during discharge, ultimately returning to the initial O3 phase at low potentials. It is important to note that due to limitations during the synchrotron experiments, we were unable to capture the diffraction patterns at the final stages of discharge (resodiation). To address this, additional *operando* laboratory XRD measurements were conducted, and the results, as shown in **Fig. S11**, confirm the reversible phase transitions of O3 → P3 and P3 → O'3. Unlike for NNTO, no O'3 (or O''3) → O1 transition is observed at potentials > 4.0 V, indicating that calcium pillaring effectively prevents structural collapse in the sodium-deficient state of CaNNTO.

Fig. 5**b** presents the volume variation associated with the different phase transitions. For easier comparison, all unit-cell volumes were converted to cubic cell volumes. The data demonstrate that the maximum change during cycling is only about 3 % for CaNNTO, representing a significant improvement over NNTO (about 30 %) [20].

Subsequently, cross-sectional SEM imaging was employed to probe the chemo-mechanical behavior of CaNNTO and NNTO. Fig. 5**c** and **e** indicates that both materials in the pristine state exhibit relatively dense structures without any visible particle fracture. However, only the secondary particles of CaNNTO are well preserved after 200 cycles (see Fig. 5**d** and **f**), revealing hardly any signs of intergranular cracking. This observation can presumably be attributed to the minor "electrode breathing" during battery operation and further suggests that the introduction of Ca^{2+} into NNTO helps mitigate mechanical degradation.

Both X-ray absorption near-edge structure (XANES) spectroscopy at the Ni and Ti K-edges and sXAS at the Ni L_3-edge were also performed to explore the redox behavior (reaction mechanism) during cycling. As

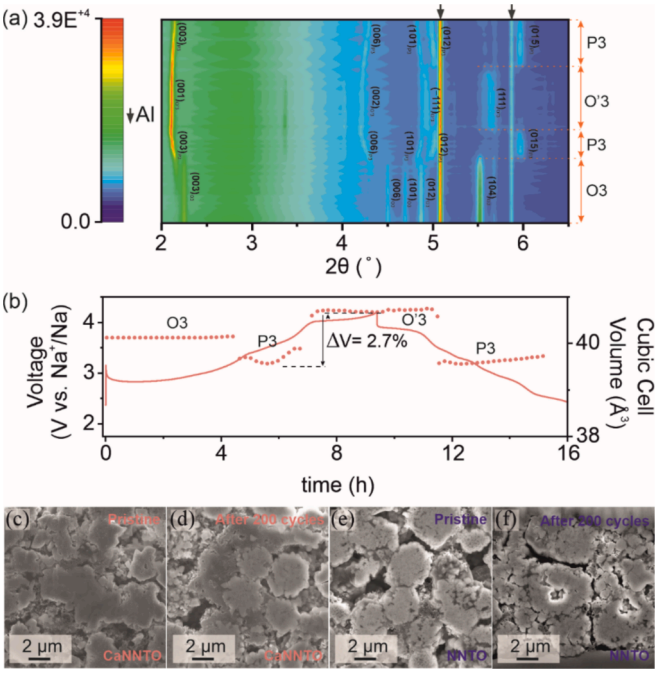

Fig. 5. (a) 2D contour plot of *operando* synchrotron XRD data collected from CaNNTO during the initial cycle at C/10 and (b) corresponding volume variation. (c–f) Cross-sectional SEM images of CaNNTO and NNTO in the pristine state and after 200 cycles at C/2.

evident from **Fig. S12a**, the Ni K-edge of pristine CaNNTO is positioned between that of NiO and NNO, indicating that nickel adopts a mixed oxidation state of Ni^{2+} and Ni^{3+}. Fig. 6**a** illustrates the evolution of the Ni K-edge in the initial cycle at a rate of C/10. As charging progresses, the spectra gradually shift to higher energies by about 3 eV, which is indicative of nickel oxidation. During discharge, the spectra shift back to the original energy position. For a more intuitive comparison, **Fig. S13a** shows the spectra recorded at open circuit voltage (OCV) and in the fully charged (4.2 V) and discharged states (2.0 V). **Fig. S12a** further presents *ex situ* spectra recorded after 20 cycles. Notably, even after 20 cycles, the spectra return to their original energy position, indicating good reversibility. By contrast, XANES data collected from NNTO reveal irreversible redox processes already after 10 cycles, highlighting that calcium pillaring has a positive effect on nickel redox, too [20]. Oxidized Ni species may migrate to the octahedral and/or tetrahedral sites (Na vacancies) in the alkali-metal layer upon cycling, [29,30] providing an explanation as to why the nickel ions in NNTO do not reach their pristine energy states after discharge. In addition, nickel migration is likely to obstruct the sodium diffusion pathways (see also **Figs. S5** and **S6**). However, the introduction of Ca^{2+} has been shown to suppress nickel migration, [30] thus ensuring fast ion transport. Aside from that, calcium pillaring helps stabilize the cathode|electrolyte interface and further enhances redox stability (see also section on DEMS below).

Figs. 6**b** and **S13b** illustrate the evolution of the Ti K-edge during the first cycle. Although slight shifts are seemingly apparent in the spectra, a comparison of first derivatives reveals no major changes, indicating that Ti^{4+} rather acts as a structural stabilizer than a redox-active ion [8,31,32]. This conclusion is further supported by the higher-quality (*ex situ*) XANES data presented in **Fig. S12b**. Note that a similar observation has been made in studies on $NaNi_{0.5}Ti_{0.5}O_2$ [32].

To examine the nickel oxidation state(s) in the bulk as well as on the surface of CaNNTO, sXAS measurements were performed *ex situ* in inverse partial fluorescence yield (IPFY) and total electron yield (TEY) modes. The Ni L_3-spectra from Massel *et al.* displayed at the bottom of Fig. 6**c** were collected from compounds in which the nickel ions are in a relatively defined oxidation state, namely NiF_2 (Ni^{2+}), K_3NiF_6 (Ni^{3+}), and $KNiIO_6$ (Ni^{4+}) [33]. Across all TEY spectra, a strong Ni^{2+} fingerprint is observed, with some indications of Ni^{3+} formation at the end of charge. This finding suggests the presence of NiO impurities on the particle surface, in agreement with the XRD results. The IPFY spectra with their much larger probing depth capture the redox behavior of the bulk material more accurately. In the pristine state, nickel is present as a mixture of Ni^{2+} and Ni^{3+}, consistent with the XANES results. With increasing desodiation, the intensity of the Ni^{2+} fingerprint strongly diminishes, while the characteristic fingerprints of Ni^{3+} and Ni^{4+} increase gradually. However, Ni^{3+} is clearly present at the end of charge (4.2 V vs. Na^+/Na), which is due to the fact that CaNNTO cannot be completely desodiated. With an actual initial specific charge capacity of 190 mAh/g, compared to the theoretical specific capacity of 226 mAh/g, about 19 % of Ni^{3+} per formula unit remain unoxidized. During discharge, CaNNTO undergoes a reversible change in intensity ratio between the high- and low-energy features, further supporting the conclusions derived from XANES analysis.

Non-destructive acoustic emission (AE) measurements were then conducted on the SIB half-cells using the CaNNTO and NNTO cathode materials. The advantage of AE testing is its ability to detect crack formation and propagation that may not be captured by XRD or other *operando* techniques [34,35]. Fig. 7 shows representative contour plots of acoustic activity (hit density) as a function of time and potential. Both CaNNTO and NNTO undergo phase transitions toward P3 and O'3 (or O''3) during cycling. However, the key differences are the absence of the O3 → O'3 transition at low potentials (about 2.5 V) and the O''3 → O1 transition at high potentials (> 4.0 V) in CaNNTO. These differences can also be noticed in the AE results. Because of the introduction of Ca^{2+}, the O^{2-}–Na^+–O^{2-} slab spacing is well maintained in the sodium-deficient state, resulting in a maximum volume change of only about 3 %,

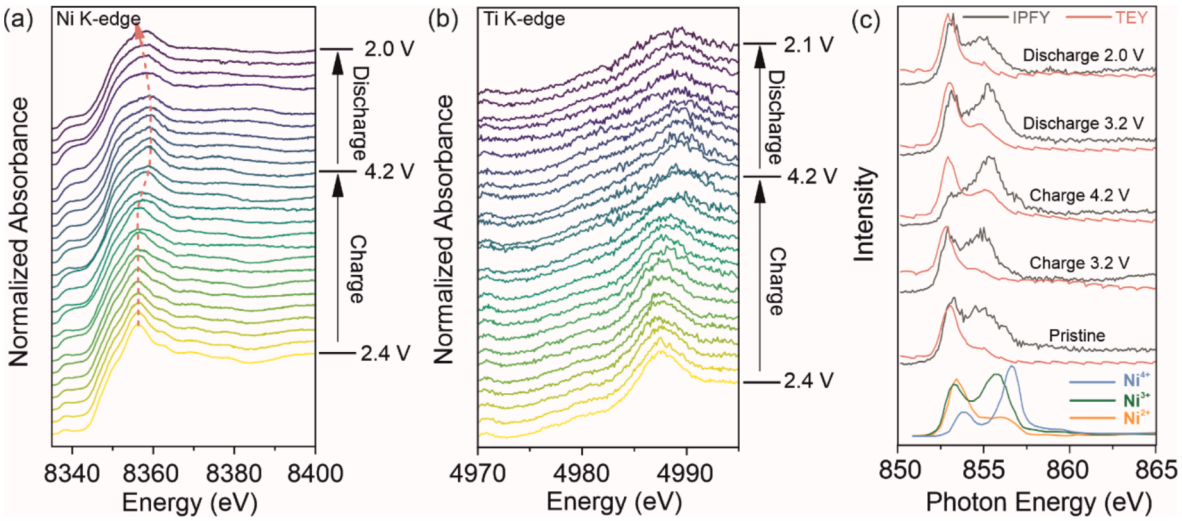

Fig. 6. (a) *In situ* XANES at the Ni K-edge and (b) Ti K-edge of CaNNTO during the initial cycle at C/10. (c) *Ex situ* Ni L_3-edge sXAS in IPFY and TEY modes of CaNNTO at different states of charge.

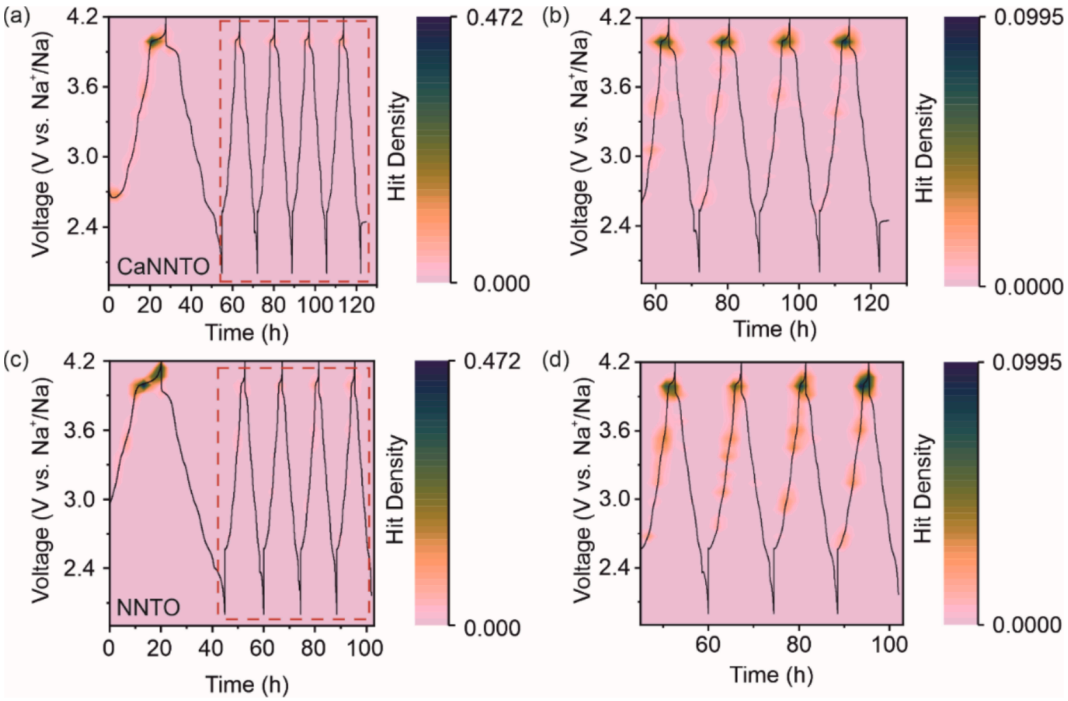

Fig. 7. Contour plots of acoustic activity (hit density) versus the time and potential for CaNNTO and NNTO. (a, c) Cycles 1–5 and (b, d) cycles 2–5.

compared to > 4 % for NNTO prior to the phase transition toward O1. As a result, even though both cathodes exhibit similar signals, the acoustic activity of CaNNTO is significantly lower than that of NNTO. The latter material shows a much higher hit density around 4.0 V, with additional signals appearing at even higher potentials. This is due to the transition to the O1 phase near 4.0 V in NNTO, which is accompanied by a 30 % volume collapse. Although CaNNTO does not undergo a phase transition at that potential, the overall small volume change still generates some acoustic activity. Aside from that, the hit density for both CaNNTO (see Fig. 7**a** and **b**) and NNTO (see Fig. 7**c** and **d**) decreases with increasing cycle number. This behavior is consistent with recent reports on P2-type SIB cathode materials, where a similar trend has been observed [36].

Finally, *in situ* gas analysis via DEMS was utilized to monitor gas evolution in the SIB half-cells during cycling operation. The cells containing either CaNNTO or NNTO were cycled in a customized setup in the same potential window of 2.0–4.2 V vs. Na^+/Na at a rate of C/10 for two cycles while simultaneously tracking the outgassing (see Fig. 8**a**–**h**). Typically, lattice oxygen is oxidized and released as reactive oxygen, which then reacts with the electrolyte to produce CO_2. Therefore, O_2 ($m/z = 32$) is often only detected in trace amounts or in the form of CO_2 [37–41]. In the case of NNTO, anionic redox activity has been suggested in previous work, and indeed, trace amounts of oxygen (about 2.9 μmol/g) are detected, whereas CaNNTO exhibits no apparent O_2 evolution. This indicates that the introduction of Ca^{2+} possibly also reduces irreversible lattice oxygen loss. As can be seen, both NNTO and CaNNTO generate H_2 ($m/z = 2$) and CO_2 ($m/z = 44$), with onset potentials of about 3.6 V. However, CaNNTO produces significantly lower amounts during the first cycle, namely 28 μmol/g of H_2 and 324 μmol/g of CO_2, compared to 59 μmol/g of H_2 and 428 μmol/g of CO_2 for NNTO. The H_2 evolution presumably stems from the reduction of protic species

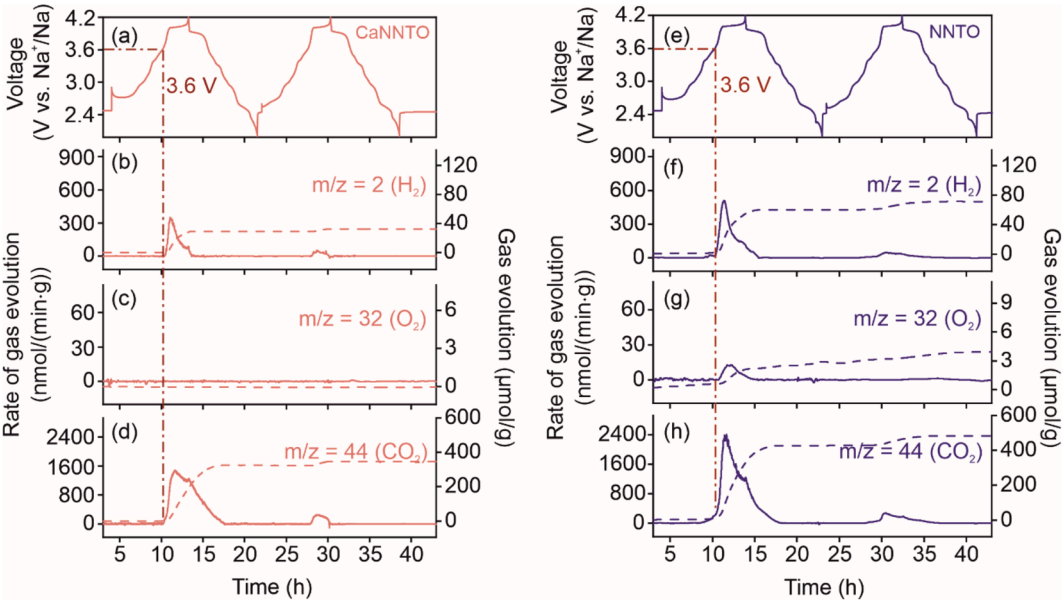

Fig. 8. (a, e) Voltage profiles at C/10 and corresponding time-resolved evolution rates (left *y*-axis) and cumulative amounts (right *y*-axis) of (b, f) H_2, (c, g) O_2, and (d, h) CO_2 measured by DEMS.

released by the oxidative electrolyte decomposition at the cathode side [42]. The lower gas evolution rates observed with CaNNTO can be attributed to several factors. One suggested contributing factor is differences in specific surface area. Another important aspect is the smaller volume variation of CaNNTO upon cycling, leading to less particle fracture and keeping the reactive surface area (available for side reactions with the electrolyte) at a minimum.

Fu *et al.* studied the effect of Ca^{2+} substitution in P2-type $Na_{0.67}Ni_{0.33}Mn_{0.67}O_2$ and found through density functional theory (DFT) calculations that it leads to an expansion of the O 2p and Ni 3d orbitals (to deeper energy levels), thereby stabilizing the electronic states of oxygen bonded to calcium. We assume that a similar effect may occur in CaNNTO [30]. Therefore, less outgassing is observed.

Irreversible lattice oxygen loss is typically accompanied by surface reconstruction, ultimately leading to the formation of a rock salt-like NiO phase, which negatively affects performance. As demonstrated by Mu *et al.*, surface nickel reduction may occur at all states of charge in sodium layered oxides [43]. Overall, the formation of NiO lowers the number of redox-active centers, causing a decrease in reversible specific capacity. Additionally, the loss of lattice oxygen may lead to a reduction in interlayer spacing. Overall, while mitigating irreversible oxygen loss, Ca^{2+} incorporation also helps maintain high redox activity and enhances the cathode|electrolyte stability.

Furthermore, O K-edge sXAS spectra were recorded in TEY mode to better understand the gassing behavior of CaNNTO. In **Fig. S14**, a peak characteristic of Na_2CO_3 (at about 534 eV) is clearly visible for both the pristine material and after charging to 3.2 V [33,44]. The presence of carbonates is also confirmed by Fourier-transform infrared (FT-IR) spectroscopy (see **Fig. S15**) [45]. However, as charging progresses to 4.2 V, the Na_2CO_3 peak vanishes, indicating that the surface carbonate species are electrochemically and/or chemically decomposed in the initial cycle. The former reaction typically produces CO_2 and O_2, while the latter may yield CO_2 and H_2O [42]. Both can contribute to the total amount of evolved CO_2 mentioned above. The peak located at about 532 eV corresponds to NiO, which further supports the XRD and Ni L_3-edge sXAS findings. In the second cycle, both CaNNTO and NNTO continue to produce H_2 and CO_2, suggesting that oxygen redox and electrolyte degradation still occur, but much less pronounced in the case of CaNNTO. It is noteworthy that the photon energy region below 534 eV typically represents the density of hole states above the Fermi level [33]. However, since the FEY mode is surface-sensitive, the information that can be gained is biased by the carbonate signal and the hole density of NiO. Nevertheless, qualitatively, the peak around 528.5 eV increases strongly during charging, likely due to oxidation reactions involving nickel.

Finally, to gain insight into the structural stability of CaNNTO and NNTO, *ex situ* XRD measurements were conducted on the cathodes both in their pristine state and after 200 cycles (see **Fig. S16**). The data provide clear evidence that both materials initially exhibit an O3-type ($R\bar{3}m$) structure. However, upon cycling, they undergo a phase transition from O3 to O'3 ($C2/m$). The key distinction is that the (001) peak shift is less pronounced [relative to the (003) peak in the pristine state] for CaNNTO, indicating that it maintains a larger interslab distance during battery operation. The smaller peak shift further suggests that more Na^+ can be reinserted into CaNNTO, which agrees with its superior performance (see **Fig. S10**). Additionally, as highlighted by the dashed box in **Fig. S16**, some fraction of O3 phase is preserved after cycling, confirming the better structural stability of CaNNTO.

In summary, Ca^{2+} was successfully introduced into the alkali-metal (intercalation) sites of NNTO, serving as pillaring ions. Cathode materials with varying Ca^{2+} contents were systematically studied, and the optimal fraction was determined to be 2.5 mol.%. XRD indicated that Ca^{2+} substitution increases the interlayer distance. Furthermore, results from *operando* XRD and AE analyses demonstrated that the issue of volume collapse at high potentials is effectively addressed by the presence of Ca^{2+}. As a result, CaNNTO exhibits strongly improved cycling performance. sXAS and XANES measurements further confirmed the superior stability of CaNNTO, while DEMS indicated that the presence of Ca^{2+} also contributes to mitigating irreversible oxygen redox and to enhancing the cathode|electrolyte stability.

Experimental section

Synthesis. $Na_{1-2x}Ca_xNi_{0.9}Ti_{0.1}O_2$, with x varying from 0.005 to 0.05, was prepared by a two-step solid-state reaction from $Ni(OH)_2$ (d_{50} ≈ 4 μm; BASF SE), nanoscale TiO_2, $Ca(OH)_2$ (Sigma-Aldrich), and NaOH (97 %; Sigma-Aldrich). For the initial pre-calcination, the reactants were homogenized under Ar atmosphere for 10 min using a laboratory blender (Kinematica). The precursor mixture was then heated in an alumina crucible under O_2 flow (7 L/h) in a tube furnace (Nabertherm

P330) at 300 °C for 10 h, with 3 K/min heating and cooling rates. After cooling to room temperature, the intermediate product was homogenized again for 10 min, followed by transfer to an alumina crucible for the main calcination under O_2 flow (7 L/h) at 800 °C for 12 h with 3 K/min heating rate and 2 K/min cooling rate.

Battery Testing. Electrodes were prepared by casting an N-methylpyrrolidone (NMP) slurry with 94 wt.% cathode material, 3 wt.% Super C65 carbon additive, and 3 wt.% polyvinylidene difluoride (PVDF, Solef 5130; Solvay) binder onto an Al foil current collector of 0.03 mm thickness. The slurry was prepared by blending the different components using 20 wt.% additional NMP in a planetary centrifuge mixer (Thinky ARE-250) at 2000 and 400 rpm, each for 3 min. The slurry was then spread onto the Al foil using a Coatmaster 510 film applicator (Erichsen) at 5 mm/s. The resultant electrodes were dried overnight at 120 °C and under dynamic vacuum, followed by calendaring at 14 N/mm (Sumet Messtechnik). Finally, 13 mm-diameter electrodes with areal loadings of 9–12 mg/cm^2 were punched out and assembled into 2032-type coin half-cells in an Ar glovebox, using GF/D glass fiber and Na metal as separator and anode, respectively. 95 µL of a 1 M solution of $NaClO_4$ in ethylene carbonate (EC), dimethyl carbonate (DMC), and propylene carbonate (PC), 1:1:1 by vol., containing 5 vol.% fluoroethylene carbonate (FEC) was used as electrolyte. In a variation, the electrolyte contained no FEC additive. Electrochemical testing was done in a potential range between 2.0 and 4.2 V vs. Na^+/Na at various current rates (1C = 200 mA/g) and with a constant voltage step at 4.2 V, either for 30 min or until the current dropped below C/100, using a battery test system (MACCOR Inc.).

Laboratory X-ray Diffraction. XRD patterns were collected from the samples in 0.5 mm-diameter borosilicate capillaries with 0.01 mm wall thickness (Hilgenberg) in Debye-Scherrer geometry using a STOE STADI-P diffractometer equipped with a DECTRIS MYTHEN 1 K strip detector and a Mo anode (λ = 0.70926 Å, 50 kV, 40 mA). The instrumental contribution to peak broadening was determined by measuring a NIST 660c LaB_6 standard as line broadening reference.

***Operando* Laboratory X-ray Diffraction.** Customized cells with Kapton windows in the center were cycled at C/20, utilizing a Gamry Interface 1000 potentiostat. XRD patterns were collected on the aforementioned STOE Stadi-P diffractometer between 5° and 37° 2θ and with an acquisition time of about 10 min.

***Operando* Synchrotron X-ray Diffraction.** Measurements were performed at the Powder Diffraction and Total Scattering beamline P02.1 at PETRA-III, DESY, Hamburg, Germany [46]. The same coin-cell design as that used in the *operando* laboratory XRD testing was employed, along with a customized holder, as detailed in the work by Herklotz *et al* [47]. The wavelength was determined to be 0.20726 Å by refinement of a NIST 660c LaB_6 standard. The electrochemical cycling was started only after recording the first pattern to ensure proper characterization of the initial material. The cells were charged and discharged galvanostatically at C/10, and XRD data were collected using the VAREX 4343CT detector (150 × 150 µm^2 pixel size, 2880 × 2880 pixel area; CsI scintillator directly deposited onto amorphous Si photodiodes) with an acquisition time of 130 s per pattern. Detector calibration was accomplished using the LaB_6 660c standard placed in the coin cell. Data integration was done using the pyFAI software, [48] and further analysis was carried out using the Rietveld method within FullProf Suite.

Scanning Electron Microscopy. SEM images were recorded at an accelerating voltage of 10 kV using a LEO-1530 microscope (Carl Zeiss AG) with a field emission source. An IB-19510CP polisher (JEOL Ltd.) with Ar source was utilized in the specimen preparation for cross-sectional imaging.

Transmission Electron Microscopy. Specimens for low-magnification TEM imaging and EDS analysis were embedded in a resin in an Ar glovebox to prevent degradation. They were cut by ultramicrotomy under dry conditions and directly investigated. During preparation, the samples were exposed to ambient air for about 10 min. Specimens for atomic resolution analysis were prepared by Ga-focused ion beam milling using a Helios 5 CX DualBeam (Thermo Fisher Scientific) and directly transferred to the microscope to minimize exposure to ambient air. They were probed using a probe-corrected Themis Z (3.1; Thermo Fisher Scientific) in HAADF STEM mode at 300 kV. The chemical composition was examined using the integrated SuperX G2 EDS detector, and the data were analyzed using the Velox 3.10 software.

Inductively Coupled Plasma-Optical Emission Spectroscopy. The elemental composition was examined by ICP-OES using an ICAP 7600 DUO (Thermo Fisher Scientific). The samples (about 10 mg) were dissolved in an acid digester within a graphite furnace, specifically in a mixture of hydrochloric acid and nitric acid at 353 K for 4 h. Mass fractions were determined from three independent measurements. The digested samples were diluted for analysis using four calibration solutions and an internal standard (Sc). Carrier gas hot extraction was employed for determining the oxygen content using a TC600 (LECO Corp.) oxygen/nitrogen analyzer and the certified standard KED-1025 for calibration.

High-energy-resolution Fluorescence Detected X-ray Absorption Near-edge Structure Spectroscopy. HERFD XANES was performed at the ID26 high brilliance X-ray spectroscopy beamline at ESRF, Grenoble, France. This beamline is an undulator beamline of high intensity. *In situ* XAS data at the Ni and Ti K-edges of CaNNTO were collected from coin cells with Kapton windows with total acquisition times of 5 and 7.5 min, respectively. The coin cells were cycled at C/10 in the potential window of 2.0–4.2 V vs. Na^+/Na and probed in HERFD mode using Si (620) for Ni and Ge (440) for Ti and a DECTRIS PILATUS 100 K detector system. For *ex situ* analysis, the pristine and cycled (two cycles at C/30 and 18 cycles at C/10) electrodes were sealed using Kapton tape in an Ar glovebox and then taken out for XANES measurements under ambient atmosphere. Multiple scans were collected for each sample to avoid beam damage. Energy calibration was done based on the first peak in the first derivative of μ(E) of Ni and Ti reference foils. All spectra were normalized and averaged (15 spectra) using the PyMca 5.9.2 software [49].

Acoustic Emission. AE signals were recorded using a differential wideband sensor (125–1000 kHz; MISTRAS Group) placed at the bottom of coin cells. The experimental setup comprised an in-line pre-amplifier and a data acquisition system (USB AE Node; MISTRAS Group). The pre-amplifier gain, analog filter, and sampling rate were set to 40 dB, 20–1000 kHz, and 5 MSPS, respectively. The sensor coupling was verified by the pencil-lead break test [20,36,50]. At least two samples were tested to ensure data reliability. Removal of background noise, using the AEwin software (MISTRAS Group), involved excluding hits of less than two counts and those with peak frequencies below 100 kHz and/or amplitudes of less than 27 dB.

Differential Electrochemical Mass Spectrometry. Customized DEMS half-cells with a 30 mm-diameter cathode of areal loading 10 mg/cm^2 were cycled at C/10. 700 µL of a 1 M solution of $NaClO_4$ in EC, DMC, and PC, 1:1:1 by vol., containing 5 vol.% FEC served as electrolyte. During cycling, a constant stream of He carrier gas (purity 6.0, 2.5 mL/min) was passed through the cell, and the extracted gas mixture was analyzed via a mass spectrometer (OmniStar GSD 320, Pfeiffer Vacuum GmbH) [51,52].

Fourier-transform Infrared Spectroscopy. Spectra were acquired on an ALPHA FT-IR spectrometer (Bruker) equipped with a Ge crystal. The measurements were performed in an Ar glovebox.

Soft X-ray Absorption Spectroscopy. sXAS measurements were performed at the ID32 beamline at ESRF, Grenoble, France [53]. The Ni L-edge was examined in TEY and IPFY modes, with an energy range from 850 to 870 eV. O K-edge XAS measurements were performed in TEY mode, with an energy range from 520 to 570 eV. IPFY spectra were recorded using the recently commissioned XES spectrometer of the ID32 beamline.

CRediT authorship contribution statement

Siyu An: Writing – original draft, Visualization, Methodology, Investigation, Formal analysis. **Leonhard Karger:** Writing – review & editing, Investigation, Formal analysis. **Philipp Müller:** Writing – review & editing, Investigation, Formal analysis. **Jing Lin:** Writing – review & editing, Investigation, Formal analysis. **Sami Vasala:** Writing – review & editing, Investigation, Formal analysis. **Volodymyr Baran:** Writing – review & editing, Investigation, Formal analysis. **Sören L. Dreyer:** Writing – review & editing, Investigation, Formal analysis. **Ruizhuo Zhang:** Writing – review & editing, Investigation, Formal analysis. **Fatih Ulusoy:** Writing – review & editing, Investigation, Formal analysis. **Aleksandr Kondrakov:** Writing – review & editing, Supervision, Project administration, Funding acquisition, Conceptualization. **Jürgen Janek:** Writing – review & editing, Supervision, Funding acquisition. **Torsten Brezesinski:** Writing – review & editing, Supervision, Project administration, Funding acquisition, Conceptualization.

Declaration of competing interest

The authors declare that they have no known competing financial interests or personal relationships that could have appeared to influence the work reported in this paper.

Acknowledgements

This study was supported by BASF SE. The authors would like to thank Thomas Bergfeldt (KIT) and Yang Hu (Helmholtz Institute Ulm) and their teams for helping collect the ICP-OES and XANES data, respectively. J. L. acknowledges the Fonds der Chemischen Industrie (FCI) for financial support. We acknowledge the ESRF for provision of synchrotron radiation facilities under proposal nos. MA-6219 (DOI: 10.15151/ESRF-ES-1550923205) and MA-6348 (DOI: 10.15151/ESRF-ES-1830838169). We also would like to thank Sami Vasala and Kurt Kummer for assistance and support in using beamlines ID26 and ID32. We acknowledge DESY, a member of the Helmholtz Association (HGF), for the provision of experimental facilities. Parts of this research were carried out at PETRA III, using beamline P02.1. Beamtime was allocated for proposal I-20230867.

Appendix A. Supplementary data

Supplementary data to this article can be found online at https://doi.org/10.1016/j.cej.2025.160939.

Data availability

Data will be made available on request.

References

[1] B. Scrosati, J. Hassoun, Y.-K. Sun, Lithium-ion batteries. A look into the future, Energy Environ. Sci. 4 (2011) 3287–3295, https://doi.org/10.1039/c1ee01388b.
[2] A. Manthiram, A reflection on lithium-ion battery cathode chemistry, Nat. Commun. 11 (2020) 1550, https://doi.org/10.1038/s41467-020-15355-0.
[3] T. Yuan, S. Li, Y. Sun, J.-H. Wang, A.-J. Chen, Q. Zheng, Y. Zhang, L. Chen, G. Nam, H. Che, J. Yang, S. Zheng, Z.-F. Ma, M. Liu, A. High-Rate, Durable Cathode for Sodium-Ion Batteries: Sb-Doped O3-Type Ni/Mn-Based Layered Oxides, ACS Nano 16 (2022) 18058–18070, https://doi.org/10.1021/acsnano.2c04702.
[4] T.-Y. Yu, J. Kim, J.-Y. Hwang, H. Kim, G. Han, H.-G. Jung, Y.-K. Sun, High-energy O3-$Na_{1-2x}Ca_x[Ni_{0.5}Mn_{0.5}]O_2$ cathodes for long-life sodium-ion batteries, J. Mater. Chem. A 8 (2020) 13776–13786, https://doi.org/10.1039/d0ta04847j.
[5] K. Chayambuka, G. Mulder, D.L. Danilov, P.H.L. Notten, Sodium-Ion Battery Materials and Electrochemical Properties Reviewed, Adv. Energy Mater. 8 (2018) 1800079, https://doi.org/10.1002/aenm.201800079.
[6] S. Li, Y. Sun, Y. Pang, S. Xia, T. Chen, H. Sun, S. Zheng, T. Yuan, Recent developments of layered transition metal oxide cathodes for sodium-ion batteries toward desired high performance, Asia-Pac. J. Chem. Eng. 17 (2022) e2762.
[7] R.-M. Gao, Z.-J. Zheng, P.-F. Wang, C.-Y. Wang, H. Ye, F.-F. Cao, Recent advances and prospects of layered transition metal oxide cathodes for sodium-ion batteries, Energy Storage Mater. 30 (2020) 9–26, https://doi.org/10.1016/j.ensm.2020.04.040.
[8] P.-F. Wang, H.-R. Yao, X.-Y. Liu, J.-N. Zhang, L. Gu, X.-Q. Yu, Y.-X. Yin, Y.-G. Guo, Ti-Substituted $NaNi_{0.5}Mn_{0.5-x}Ti_xO_2$ Cathodes with Reversible O3−P3 Phase Transition for High-Performance Sodium-Ion Batteries, Adv. Mater. 29 (2017) 1700210, https://doi.org/10.1002/adma.201700210.
[9] S. Guo, H. Yu, P. Liu, Y. Ren, T. Zhang, M. Chen, M. Ishida, H. Zhou, High-performance symmetric sodium-ion batteries using a new, bipolar O3-type material, $Na_{0.8}Ni_{0.4}Ti_{0.6}O_2$, Energy Environ. Sci. 8 (2015) 1237–1244, https://doi.org/10.1039/c4ee03361b.
[10] P.-F. Wang, Y. You, Y.-X. Yin, Y.-S. Wang, L.-J. Wan, L. Gu, Y.-G. Guo, Suppressing the P2–O2 Phase Transition of $Na_{0.67}Mn_{0.67}Ni_{0.33}O_2$ by Magnesium Substitution for Improved Sodium-Ion Batteries, Angew. Chem., Int. Ed. 128 (2016) 7571–7575, https://doi.org/10.1002/ange.201602202.
[11] M.H. Han, E. Gonzalo, G. Singh, T. Rojo, A comprehensive review of sodium layered oxides: powerful cathodes for Na-ion batteries, Energy Environ. Sci. 8 (2015) 81–102, https://doi.org/10.1039/c4ee03192j.
[12] X. Li, Y. Wang, D. Wu, L. Liu, S.-H. Bo, G. Ceder, Jahn–Teller Assisted Na Diffusion for High Performance Na Ion Batteries, Chem. Mater. 28 (2016) 6575–6583, https://doi.org/10.1021/acs.chemmater.6b02440.
[13] S. Kim, X. Ma, S.P. Ong, G. Ceder, A comparison of destabilization mechanisms of the layered Na_xMO_2 and Li_xMO_2 compounds upon alkali de-intercalation, Phys. Chem. Chem. Phys. 14 (2012) 15571–15578, https://doi.org/10.1039/c2cp43377j.
[14] C. Delmas, C. Fouassier, P. Hagenmuller, Structural classification and properties of the layered oxides, Physica b+c 99 (1980) 81–85, https://doi.org/10.1016/0378-4363(80)90214-4.
[15] C. Delmas, J.-J. Braconnier, C. Fouassier, P. Hagenmuller, Electrochemical intercalation of sodium in Na_xCoO_2 bronzes, Solid State Ion. 3–4 (1981) 165–169, https://doi.org/10.1016/0167-2738(81)90076-X.
[16] J.-H. Kim, H.-H. Ryu, S.J. Kim, C.S. Yoon, Y.-K. Sun, Degradation Mechanism of Highly Ni-Rich $Li[Ni_xCo_yMn_{1-x-y}]O_2$ Cathodes with $x > 0.9$, ACS Appl, Mater. Interfaces 11 (2019) 30936–30942, https://doi.org/10.1021/acsami.9b09754.
[17] H.-H. Ryu, K.-J. Park, C.S. Yoon, Y.-K. Sun, Capacity Fading of Ni-Rich Li $[Ni_xCo_yMn_{1-x-y}]O_2$ ($0.6 \leq x \leq 0.95$) Cathodes for High-Energy-Density Lithium-Ion Batteries: Bulk or Surface Degradation? Chem. Mater. 30 (2018) 1155–1163, https://doi.org/10.1021/acs.chemmater.7b05269.
[18] G.W. Nam, N.-Y. Park, K.-J. Park, J. Yang, J. Liu, C.S. Yoon, Y.-K. Sun, Capacity Fading of Ni-Rich NCA Cathodes: Effect of Microcracking Extent, ACS Energy Lett. 4 (2019) 2995–3001, https://doi.org/10.1021/acsenergylett.9b02302.
[19] T.-Y. Yu, H.-H. Ryu, G. Han, Y.-K. Sun, Understanding the Capacity Fading Mechanisms of O3-Type $Na[Ni_{0.5}Mn_{0.5}]O_2$ Cathode for Sodium-Ion Batteries, Adv. Energy Mater. 10 (2020) 2001609, https://doi.org/10.1002/aenm.202001609.
[20] S. An, L. Karger, S.L. Dreyer, Y. Hu, E. Barbosa, R. Zhang, L. Jing, M. Fichtner, A. Kondrakov, J. Janek, T. Brezesinski, Improving cycling performance of the $NaNiO_2$ cathode in sodium-ion batteries by titanium substitution, Mater. Futures 3 (2024) 035103, https://doi.org/10.1088/2752-5724/ad5faa.
[21] L. Sun, Y. Xie, X.-Z. Liao, H. Wang, G. Tan, Z. Chen, Y. Ren, J. Gim, W. Tang, Y.-S. He, K. Amine, Z.-F. Ma, Insight into Ca-Substitution Effects on O3-Type $NaNi_{1/3}Fe_{1/3}Mn_{1/3}O_2$ Cathode Materials for Sodium-Ion Batteries Application, Small 14 (2018) 1704523, https://doi.org/10.1002/smll.201704523.
[22] Q. Tao, H. Ding, H. Zhao, J. Huang, B. Dai, J. Li, Ca-doped Na-site $NaNi_{1/3}Fe_{1/3}Mn_{1/3}O_2$ as a high-performance cathode material for sodium ion batteries, J. Alloys Compd. 976 (2024) 172977, https://doi.org/10.1016/j.jallcom.2023.172977.
[23] M. Matsui, F. Mizukoshi, H. Hasegawa, N. Imanishi, Ca-substituted P3-type $Na_xNi_{1/3}Mn_{1/3}Co_{1/3}O_2$ as a potential high voltage cathode active material for sodium-ion batteries, J. Power Sources 485 (2021) 229346, https://doi.org/10.1016/j.jpowsour.2020.229346.
[24] J. Zhou, Y. Zhang, W. Xu, X. Li, W. Zhou, W. Zhang, N. Wang, M. Liu, K. Dai, Enhancing electrochemical performance of sodium-ion batteries: Optimal Ca^{2+} doping in O3-$NaNi_{0.33}Mn_{0.33}Fe_{0.33}O_2$ layered oxide cathode materials, J. Electroanal. Chem. 969 (2024) 118541, https://doi.org/10.1016/j.jelechem.2024.118541.
[25] S.-B. Wei, Y.-J. He, Y. Tang, H.-W. Fu, J. Zhou, S.-Q. Liang, X.-X. Cao, A Ca-substituted air-stable layered oxide cathode material with facilitated phase transitions for high-performance Na-ion batteries, Rare Met. 43 (2024) 5701–5711, https://doi.org/10.1007/s12598-024-02819-1.
[26] L. Zhang, J. Deshmukh, H. Hijazi, Z. Ye, M.B. Johnson, A. George, J.R. Dahn, M. Metzger, Impact of Calcium on Air Stability of $Na[Ni_{1/3}Fe_{1/3}Mn_{1/3}]O_2$ Positive Electrode Material for Sodium-ion Batteries, J. Electrochem. Soc. 170 (2023) 070514, https://doi.org/10.1149/1945-7111/ace55a.
[27] M. Matsui, F. Mizukoshi, N. Imanishi, Improved cycling performance of P2-type layered sodium cobalt oxide by calcium substitution, J. Power Sources 280 (2015) 205–209, https://doi.org/10.1016/j.jpowsour.2015.01.044.
[28] S.C. Han, H. Lim, J. Jeong, D. Ahn, W.B. Park, K.-S. Sohn, M. Pyo, Ca-doped Na_xCoO_2 for improved cyclability in sodium ion batteries, J. Power Sources 277 (2015) 9–16, https://doi.org/10.1016/j.jpowsour.2014.11.150.
[29] L. Wang, J. Wang, X. Zhang, Y. Ren, P. Zuo, G. Yin, J. Wang, Unravelling the origin of irreversible capacity loss in $NaNiO_2$ for high voltage sodium ion batteries, Nano Energy 34 (2017) 215–223, https://doi.org/10.1016/j.nanoen.2017.02.046.
[30] H. Fu, Y.-P. Wang, G. Fan, S. Guo, X. Xie, X. Cao, B. Lu, M. Long, J. Zhou, S. Liang, Synergetic stability enhancement with magnesium and calcium ion substitution for Ni/Mn-based P2-type sodium-ion battery cathodes, Chem. Sci. 13 (2022) 726–736, https://doi.org/10.1039/d1sc05715d.

[31] K. Kubota, N. Fujitani, Y. Yoda, K. Kuroki, Y. Tokita, S. Komaba, Impact of Mg and Ti doping in O3 type $NaNi_{1/2}Mn_{1/2}O_2$ on reversibility and phase transition during electrochemical Na intercalation, J. Mater. Chem. A 9 (2021) 12830–12844, https://doi.org/10.1039/D1TA01164B.
[32] S. Maletti, A. Sarapulova, A. Schökel, D. Mikhailova, Operando Studies on the $NaNi_{0.5}Ti_{0.5}O_2$ Cathode for Na-Ion Batteries: Elucidating Titanium as a Structure Stabilizer, ACS Appl. Mater. Interfaces 11 (2019) 33923–33930, https://doi.org/10.1021/acsami.9b10352.
[33] F. Massel, B. Aktekin, Y.-S. Liu, J. Guo, M.H. Sørby, D. Brandell, R. Younesi, M. Hahlin, L.-C. Duda, The role of anionic processes in $Li_{1-x}Ni_{0.44}Mn_{1.56}O_4$ studied by resonant inelastic X-ray scattering, Energy Adv. 2 (2023) 375–384, https://doi.org/10.1039/d2ya00321j.
[34] M. Enoki H. Inaba Y. Mizutani N. Nakano M. Ohtsu, Practical Acoustic Emission Testing (2016) Tokyo: Springer, doi:10.1007/978-4-431-55072-3.
[35] S. Schweidler, M. Bianchini, P. Hartmann, T. Brezesinski, J. Janek, The Sound of Batteries: An Operando Acoustic Emission Study of the $LiNiO_2$ Cathode in Li–Ion Cells, Batteries Supercaps 3 (2020) 1021–1027, https://doi.org/10.1002/batt.202000099.
[36] S.L. Dreyer, R. Zhang, J. Wang, A. Kondrakov, Q. Wang, T. Brezesinski, J. Janek, The effect of configurational entropy on acoustic emission of P2-type layered oxide cathodes for sodium-ion batteries, J. Phys. Energy 5 (2023) 035002, https://doi.org/10.1088/2515-7655/acd41a.
[37] R. Jung, M. Metzger, F. Maglia, C. Stinner, H.A. Gasteiger, Oxygen Release and Its Effect on the Cycling Stability of $LiNi_xMn_yCo_zO_2$ (NMC) Cathode Materials for Li-Ion Batteries, J. Electrochem. Soc. 164 (2017) A1361–A1377, https://doi.org/10.1149/2.0021707jes.
[38] J. Wandt, A.T.S. Freiberg, A. Ogrodnik, H.A. Gasteiger, Singlet oxygen evolution from layered transition metal oxide cathode materials and its implications for lithium-ion batteries, Mater. Today 21 (2018) 825–833, https://doi.org/10.1016/j.mattod.2018.03.037.
[39] R. Jung, M. Metzger, F. Maglia, C. Stinner, H.A. Gasteiger, Chemical versus Electrochemical Electrolyte Oxidation on NMC111, NMC622, NMC811, LNMO, and Conductive Carbon, J. Phys. Chem. Lett. 8 (2017) 4820–4825, https://doi.org/10.1021/acs.jpclett.7b01927.
[40] J.K. Papp, N. Li, L.A. Kaufman, A.J. Naylor, R. Younesi, W. Tong, B.D. McCloskey, A comparison of high voltage outgassing of $LiCoO_2$, $LiNiO_2$, and Li_2MnO_3 layered Li-ion cathode materials, Electrochim. Acta 368 (2021) 137505, https://doi.org/10.1016/j.electacta.2020.137505.
[41] S.L. Dreyer, A. Kondrakov, J. Janek, T. Brezesinski, In situ analysis of gas evolution in liquid- and solid-electrolyte-based batteries with current and next-generation cathode materials, J. Mater. Res. 37 (2022) 3146–3168, https://doi.org/10.1557/s43578-022-00586-2.
[42] L. Zhang, C. Tsolakidou, S. Mariyappan, J.-M. Tarascon, S. Trabesinger, Unraveling gas evolution in sodium batteries by online electrochemical mass spectrometry, Energy Storage Mater. 42 (2021) 12–21, https://doi.org/10.1016/j.ensm.2021.07.005.
[43] L. Mu, X. Feng, R. Kou, Y. Zhang, H. Guo, C. Tian, C.-J. Sun, X.-W. Du, D. Nordlund, H.L. Xin, F. Lin, Deciphering the Cathode–Electrolyte Interfacial Chemistry in Sodium Layered Cathode Materials, Adv. Energy Mater. 8 (2018) 1801975, https://doi.org/10.1002/aenm.201801975.
[44] I. Moeez, D. Susanto, W. Chang, H.-D. Lim, K.Y. Chung, Artificial cathode electrolyte interphase by functional additives toward long-life sodium-ion batteries, Chem. Eng. J. 425 (2021) 130547, https://doi.org/10.1016/j.cej.2021.130547.
[45] T. Hatsukade, A. Schiele, P. Hartmann, T. Brezesinski, J. Janek, Origin of Carbon Dioxide Evolved during Cycling of Nickel-Rich Layered NCM Cathodes, ACS Appl. Mater. Interfaces 10 (2018) 38892–38899, https://doi.org/10.1021/acsami.8b13158.
[46] A.-C. Dippel, H.-P. Liermann, J.T. Delitz, P. Walter, H. Schulte-Schrepping, O. H. Seeck, H. Franz, Beamline P02.1 at PETRA III for high-resolution and high-energy powder diffraction, J. Synchrotron Radiat. 22 (2015) 675–687, https://doi.org/10.1107/S1600577515002222.
[47] M. Herklotz, J. Weiß, E. Ahrens, M. Yavuz, L. Mereacre, N. Kiziltas-Yavuz, C. Dräger, H. Ehrenberg, J. Eckert, F. Fauth, L. Giebeler, M. Knapp, A novel high-throughput setup for in situ powder diffraction on coin cell batteries, J. Appl. Cryst. 49 (2016) 340–345, https://doi.org/10.1107/S1600576715022165.
[48] G. Ashiotis, A. Deschildre, Z. Nawaz, J.P. Wright, D. Karkoulis, F.E. Picca, J. Kieffer, The fast azimuthal integration Python library: PyFAI, J. Appl. Cryst. 48 (2015) 510–519, https://doi.org/10.1107/S1600576715004306.
[49] V.A. Solé, E. Papillon, M. Cotte, Ph. Walter, J. Susini, A multiplatform code for the analysis of energy-dispersive X-ray fluorescence spectra, Spectrochim. Acta Part B, At. Spectrosc. 62 (2007) 63–68, https://doi.org/10.1016/j.sab.2006.12.002.
[50] S. Schweidler, S.L. Dreyer, B. Breitung, T. Brezesinski, Operando acoustic emission monitoring of degradation processes in lithium-ion batteries with a high-entropy oxide anode, Sci. Rep. 11 (2021) 23381, https://doi.org/10.1038/s41598-021-02685-2.
[51] B.B. Berkes, A. Jozwiuk, H. Sommer, T. Brezesinski, J. Janek, Simultaneous acquisition of differential electrochemical mass spectrometry and infrared spectroscopy data for in situ characterization of gas evolution reactions in lithium-ion batteries, Electrochem. Commun. 60 (2015) 64–69, https://doi.org/10.1016/j.elecom.2015.08.002.
[52] B.B. Berkes, A. Jozwiuk, M. Vračar, H. Sommer, T. Brezesinski, J. Janek, Online Continuous Flow Differential Electrochemical Mass Spectrometry with a Realistic Battery Setup for High-Precision, Long-Term Cycling Tests, Anal. Chem. 87 (2015) 5878–5883, https://doi.org/10.1021/acs.analchem.5b01237.
[53] N.B. Brookes, F. Yakhou-Harris, K. Kummer, A. Fondacaro, J.C. Cezar, D. Betto, E. Velez-Fort, A. Amorese, G. Ghiringhelli, L. Braicovich, R. Barrett, G. Berruyer, F. Cianciosi, L. Eybert, P. Marion, P. van der Linden, L. Zhang, The beamline ID32 at the ESRF for soft X-ray high energy resolution resonant inelastic X-ray scattering and polarisation dependent X-ray absorption spectroscopy, Nucl. Instrum. Methods Phys. Res., Sect. A 903 (2018) 175–192, https://doi.org/10.1016/j.nima.2018.07.001.